Materials Today Nano 30 (2025) 100621

Contents lists available at ScienceDirect

Materials Today Nano

journal homepage: www.sciencedirect.com/journal/materials-today-nano

A new Fe-based nanocrystalline soft magnetic composites with ultra-low core loss and superior DC-bias permeability up to megahertz-frequency

Zhijun Guo, Xingyu Zheng, Changlong Jin, Yanzhou Fan, Mingjuan Cai, Jifeng Zhou, Wanying Dong, Qiang Luo *, Baolong Shen **

School of Materials Science and Engineering, Jiangsu Key Laboratory for Advanced Metallic Materials, Southeast University, Nanjing, 211189, China

ARTICLE INFO

Keywords:
Soft magnetic composites (SMCs)
Fe-based nanocrystalline powder
Low core loss
High DC-Bias stability
High-frequency property

ABSTRACT

Demands on soft magnetic composites (SMCs) for superior magnetic performance, including low core loss, high permeability, high saturation magnetic flux density, and strong DC-bias stability up to dozes of megahertz, are urgently needed for power electronics, which are crucial in advancing third-generation semiconductors. However, traditional SMCs systems face challenges of high loss and poor DC-bias characteristics. In the present study, high-performance SMCs were fabricated by novel $Fe_{73.3}P_5Si_{7.6}B_{9.5}C_{1.9}Nb_2Cu_{0.7}$ powders with spherical shapes and a fully glassy structure, which were produced *via* gas atomization. To enhance the magnetic performance at high frequencies, in-situ oxide insulation layers were formed by controlling the varying concentrations of HNO_3. The evolution of the oxidation layer's structure and thickness was systematically clarified. SMCs demonstrated superior magnetic performance, including highly stable permeability (μ') remained between 30 and 47 up to 20 MHz, excellent DC-bias permeability increase from 57.8 % to 82.7 % under 100 Oe, high cut-off frequency up to 96 MHz, and low core loss (P_{cv}) that regulated less than 153–173 mW/cm^3 (50 mT, 100 kHz), 590–663 mW/cm^3 (100 mT, 100 kHz). The magnetic properties of present SMCs are comparable to those of the most prominent SMCs reported so far. The proposed method and alloy composition provide a promising pathway for producing advanced SMCs. These results are meaningful for potentially stimulating the development and application of new low-loss SMCs.

1. Introduction

The advancement of third-generation powder semiconductors is driving power electronics towards higher working frequency (<10 MHz) and high power density [1]. Compared to traditional soft magnetic materials, SMCs offer significant advantages in high-frequency applications due to their ability to reduce eddy current losses, provide tailored magnetic properties, enable efficient designs, and resist the DC-bias et al. [2–4]. DC-bias performance of SMCs is an essential property for high-power devices since the non-negligible pre-magnetization occurs under a large DC component [5]. The high DC-bias performance can significantly ensure sufficient high μ_e and low P_{cv} under a large DC field. At present, the typical commercial SMCs mainly include Fe, FeSi, FeSiAl, FeNi and FeNiMo with DC-bias (100 Oe) value of 40–70, 63–76, 40–50, 68–80, 50–55, respectively [6]. However, these typical commercial SMCs encounter challenges related to poor DC-bias performance along with high P_{cv} and weak stability [7,8]. A common way to enhance the DC-bias performance is to select materials with High B_s, optimized magnetic anisotropy, reduced coercivity (H_c), and minimized magnetostriction (λ_s). Amongst the numerous soft magnetic powders [7,9], the Fe-based nanocrystalline alloys have exhibited superior overall soft-magnetic properties and are attractive for high-frequency applications. Their unique dual-phase nanocrystalline/amorphous structure enables lower magnetic losses and superior temperature stability, which enhances DC-bias performance, making them suitable for high-frequency applications [10,11].Among these, the Finemet-type alloys (Fe-Si-Nb-B-Cu) have dominated commercial applications since the 1990s, achieving B_s ~1.24 T with modest GFA. However, their performance ceiling has remained largely unchallenged for decades, constrained by the inherent trade-off between B_s enhancement and GFA deterioration in conventional composition design paradigms. Currently, research aimed at enhancing the performances of

* Corresponding author.
** Corresponding author.
E-mail addresses: q.luo@seu.edu.cn (Q. Luo), blshen@seu.edu.cn (B. Shen).

https://doi.org/10.1016/j.mtnano.2025.100621
Received 1 March 2025; Received in revised form 1 April 2025; Accepted 9 April 2025
Available online 11 April 2025

Fe-based nanocrystalline SMCs often employs two strategies. One is to design and develop new compositions of nanocrystalline powders, such as Finemet [12], $Fe_{84.8}Si_{0.5}B_{9.4}P_{3.5}C_1Cu_{0.8}$ [13], and $Fe_{85.5}B_{10}Si_2P_2C_{0.5}$ [14], which have high B_s and low H_c. The second is to tailor the physical and chemical properties of the insulation layers. The high-quality insulating layer can increase resistivity and suppress eddy current losses [15]. Achieving optimal magnetic performance requires insulation layers with high thermal stability, strong adhesion, and minimal magnetic dilution effects. Organic coatings are often limited by their low decomposition temperatures, which restrict their application in high-temperature environments [16]. Inorganic coatings, though more resilient, are prone to cracking during cold compaction, compromising insulation quality and degrading magnetic performance [17,18]. Recent studies have explored in-situ oxidation methods to form insulating layers directly on magnetic powder surfaces, offering superior adhesion and thermal stability. The ferrimagnetic Fe_3O_4 coatings formed *via* in-situ oxidation have shown particular promise by reducing eddy current losses without significantly compromising magnetic properties [19,20]. However, these methods have faced challenges related to uniformity, scalability, and the magnetic dilution effect of non-magnetic oxides such as Fe_2O_3. Therefore, exploring a new type of Fe-based nanocrystalline and high-performance insulation layer is a valuable research direction.

To address these limitations, in this study, we developed a novel FePSiBCNbCu nanocrystalline with higher B_s (1.36 T) and GFA (~1.5 mm) than Finemet. The spherical powders were successfully prepared by gas atomization with a fully amorphous structure. Afterwards, in-situ oxide insulation layers were introduced by oxidized with varying concentrations of HNO_3. The evolution of the oxidation layer's structure and thickness was systematically clarified. The correlation among hysteresis loss (P_h), eddy current loss (P_e) and excess loss (P_{exc}), permeability (μ), DC-bias performance and the internal microstructure of these SMCs have been systematically studied. The mechanism underlying the effects of the in-situ insulation layer on the high-frequency performance of SMCs was also elucidated. Notably, the SMCs prepared from FePSiBCNbCu nanocrystalline powder possess the optimum combination of low P_{cv}, high cut-off frequency, and high DC-bias performance [21,22].

2. Experimental procedures

Alloy ingots with nominal compositions of $Fe_{75.3-x}P_5Si_{7.6}B_{9.5}C_{1.9}Nb_xCu_{0.7}$ (x = 0, 1, 2 and 3 at. %) were prepared by induction melting the high-purity metals of Fe (99.99 wt%), B (99.99 wt %), Si (99.999 wt%), Nb (99.99 wt%) Cu (99.99 wt%), and pre-alloys of Fe-P (26.4 wt% P) and Fe-C (5 wt% C) under an argon atmosphere. Subsequently, the cylindrical rods with diameters up to 1.5 mm, of which were shaped to consider amorphous formability, were produced through the Cu-mold casting, and the as-quenched (AQ) ribbons were produced *via* a single-roller melt-spinning with a thickness of 20 μm. Differential scanning calorimetry (DSC) was employed at 40 °C/min heating rate under flowing argon gas to determine the appropriate annealing temperature (T_a) range for nanocrystallization. Before magnetic performance evaluation, the ribbons were annealed at temperatures ranging from 460 to 540 °C for 30 min in an argon atmosphere. Considering GFA and soft magnetic properties, $Fe_{73.3}P_5Si_{7.6}B_{9.5}C_{1.9}Nb_2Cu_{0.7}$ powder was prepared through gas atomization. The molten alloy was dispersed and rapidly cooled by a high-pressure argon gas flow, with the atomization pressure maintained at 7.5 MPa. To prepare insulating layers, the amorphous powders after 200-mesh sieve were dispersed in HNO_3-ethanol solution (5 wt%, 10 wt%, and 20 wt%) under continuous stirring for 10 min. For the convenience of description, AMPO-n (n = 5, 10, 20) represents the atomized $Fe_{73.3}P_5Si_{7.6}B_{9.5}C_{1.9}Nb_2Cu_{0.7}$ powder treated by n wt% HNO_3, and raw powder denotes AMPC. The oxidized powders were mixed with 2 wt% epoxy resin (EP) to ensure particle adhesion and improve the insulation properties between individual powder particles. The composite powders were compressed into ring-shaped samples (outer diameter: 12.7 mm, inner diameter: 7.6 mm) by cold pressing under a uniaxial pressure of 1800 MPa for 60 s. Finally, these compacted samples were sealed in vacuum quartz tubes and annealed at 480 °C for 30 min to induce nanocrystallization. For the convenience of description, SMCC and SMCO-n (n = 5, 10, 20) represent magnetic core compressed with AMPC and AMPO-n, respectively. The GFA of $Fe_{75.3-x}P_5Si_{7.6}B_{9.5}C_{1.9}Nb_xCu_{0.7}$ nanocrystalline alloys and fabrication of the schematic process are detailed in Fig. 1.

The phase structures of the original and oxidized powders were analyzed using X-ray diffraction (XRD, Bruker D8 Focus). The microstructure and element composition of the powders and the SMCs were investigated using a scanning electron microscope (SEM, Zeiss Rossbeam350) equipped with an energy dispersive spectrometer (EDS). To investigate the chemical state and valence states of the oxidation layers, fourier transform infrared spectrometer (FTIR, Thermo Scientific Nicolet iS10) and X-ray photoelectron spectroscopy (XPS, Thermo Scientific ESCALAB 250Xi) were employed. The detailed microstructure and composition of the powders, along with the oxidation layers, were observed using transmission electron microscopy (TEM, Thermo Scientific Talos F200X) equipped with selected area electron diffraction (SAED) and energy-dispersive X-ray spectroscopy (EDS). The TEM samples were prepared by depositing a Pt-protecting layer on the oxidation layer of the SMCs prior to trench milling around a small region using a focused ion beam (FIB). The hysteresis loops of the SMCs were measured by a vibrating sample magnetometer (VSM, Lakeshore 707) under an applied magnetic field up to 800 kA/m. An impedance analyzer (Keysight, E4990A) was utilized to assess the complex permeability of the SMCs over a frequency range of 10 kHz–120 MHz. Additionally, an LCR meter (TongHui TH2828A) was employed to determine the percentage of magnetic permeability (μ_e%) under DC magnetization fields up to 100 Oe. P_{cv} in the frequency range of 10 kHz-1 MHz was measured by B-H analyzer (SY-8218, IWATSU). The resistivity of SMCs was quantified with an ultra-high resistance tester (ST2643).

3. Results and discussion

3.1. Magnetic performance of the SMCO-n

The variation in complex permeability spectra of SMCC and SMCO-n are presented in Fig. 2(a and b). All samples maintain excellent frequency stability across the range of 10 kHz–20 MHz, ensuring reliable operation under high-frequency conditions. Although the permeability of the SMCO-n decreases compared to the SMCC, it remains over 30 up to 30 MHz, demonstrating retention of expected magnetic properties. The SMCO-5 shows the lowest permeability. Conversely, SMCO-10 and SMCO-20 exhibit higher permeability, which may result from the different structures of the insulation layer that affect demagnetizing fields [23]. The imaginary permeability (μ'') spectra in Fig. 2b reflect the energy loss during magnetization. As frequency increases, μ'' initially rises, reaching a peak at the cut-off frequency, which signifies the material's upper operational limit and the point of maximum energy dissipation [24]. The cut-off frequency of the SMCO-n shifts to higher values than the SMCC, indicating an expanded operational frequency range. Especially, SMCO-20 achieves the highest cut-off frequency of 96 MHz. The DC-bias performance assesses the material's ability to maintain permeability under high DC-bias fields—an essential metric for evaluating the performance of soft magnetic composites in high-current applications [25]. As is shown in Fig. 2c, the permeability of all samples gradually declines due to magnetic saturation as the DC-bias field increases. SMCO-10 and SMCO-20 achieve significantly improved DC-bias retention of 73.2 % and 82.7 % compared to SMCC of 57.9 % under 100 Oe. In addition, P_{cv} is a critical magnetic property influencing the efficiency of SMCs, particularly in high-frequency applications. Minimizing P_{cv} is essential to enhance the energy conversion efficiency of devices [26,27]. The dependence of P_{cv} on frequency (10 kHz–1 MHz) at

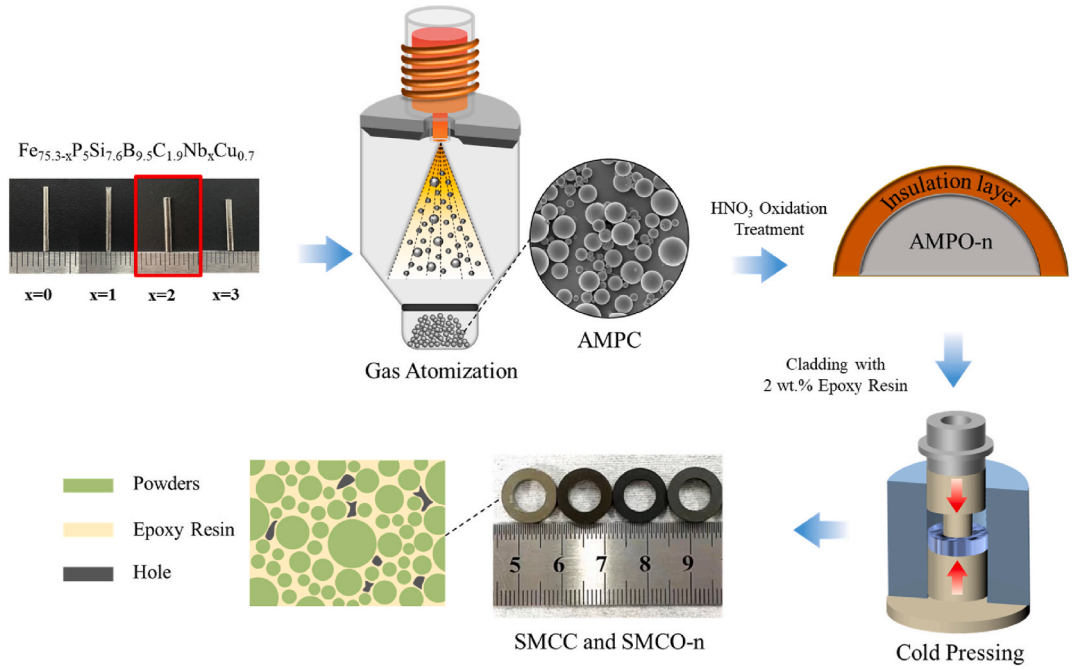

Fig. 1. GFA of $Fe_{75.3-x}P_5Si_{7.6}B_{9.5}C_{1.9}Nb_xCu_{0.7}$ (x = 0, 1, 2 and 3) nanocrystalline alloys and schematic diagram illustrating the preparation process of the SMCC and SMCO-n.

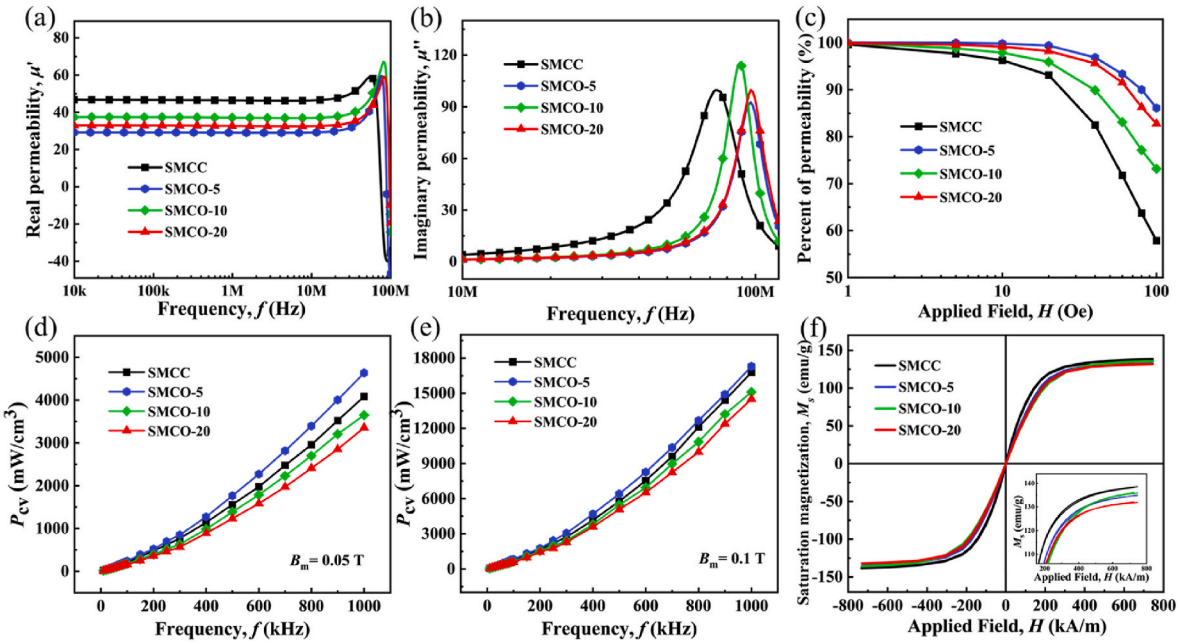

Fig. 2. Magnetic performance of SMCC and SMCO-n: (a) μ' and (b) μ'' as a function of the frequency, (c) percent of permeability as a function of the DC magnetizing field, (d) P_{cv} as a function of the frequency at 0.05 T, (e) P_{cv} as a function of the frequency at 0.01 T, (f) magnetization curves of SMCC and SMCO-n.

magnetic inductions (B_m) of 0.05 T and 0.1 T for SMCC and SMCO-n are presented in Fig. 2d, e. Across all samples, P_{cv} experiences an increase trend with both frequency and B_m increase; however, the growth rate varies significantly among samples. Specifically, SMCO-20 demonstrates the lowest P_{cv} with values reduced to 153 mW/cm^3 (0.05 T, 100 kHz) and 590 mW/cm^3 (0.1 T, 100 kHz), approximately 27 % and 20 % lower than SMCC, whereas the SMCO-5 exhibits the highest value of P_{cv}. Fig. 2f shows the hysteresis loops of the samples. The saturation magnetization (M_s) of SMCO-n ranges from 131 to 136 emu/g, slightly lower than that of SMCC. This reduction reflects the magnetic dilution effect induced by the formation of phases/composites within the insulation layer.

In terms of SMCs, high DC-bias capacity ensures stable magnetic permeability and performance under superimposed DC fields, while low core loss reduces energy dissipation and heat generation at high frequencies. These attributes collectively enhance the efficiency, thermal stability, and reliability of SMCs, making them ideal for compact, high-frequency applications [1]. Fig. 3 summarized P_{cv} and DC-bias performance of the reported typical Fe-based amorphous/nanocrystalline as well as widely used FeSiAl SMCs [28,29]. It shows that the SMCO-10 and SMCO-20 developed in this work exhibit superior performance, of which

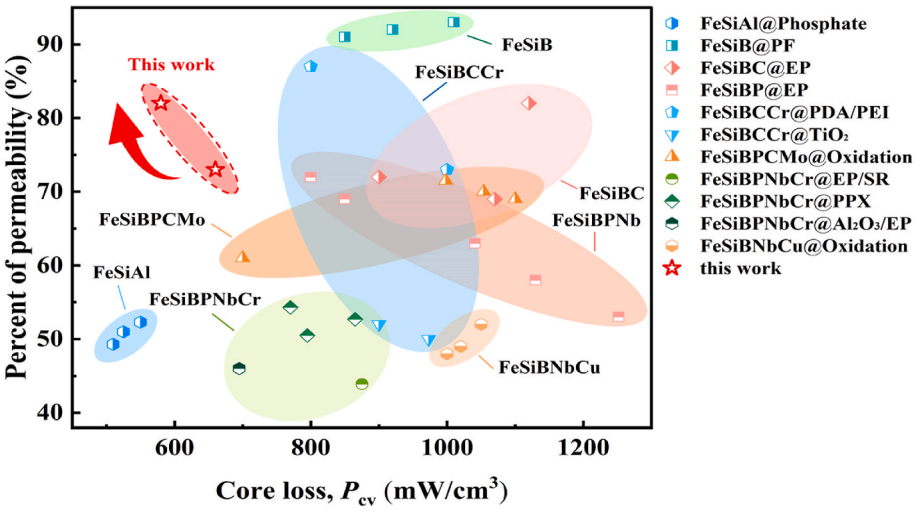

Fig. 3. Comparison of the core loss P_{cv} (0.1 T, 100 kHz) and DC bias performance (100 Oe) obtained in this work and previous literature reported for different SMCs types.

P_{cv} is significantly lower, while the DC-bias is extremely higher than many advanced counterparts, indicating enhanced energy efficiency and stability suitable for application in electronic components.

3.2. Microstructure analysis of ribbon and atomized powders

The composition of the amorphous nanocrystalline alloy is the key to achieving the superior magnetic performance of SMCs, such as low core loss, high permeability, high saturation magnetic flux density, etc. Thus, the alloy's composition selection is critical to obtaining the powders with comprehensive magnetic and high GFA properties. AQ ribbons with different Nb content show the amorphous structure, as shown in Fig. 4a without a detectable shift of diffraction hump. Moreover, with increasing Nb content, the crystallization onset temperature (T_{x1}) exhibits a modest increase, while the second crystallization temperature (T_{x2}) shifts significantly to a higher temperature (Fig. 4b). This shift suggests an expansion of the heat treatment window, facilitating better control over the crystallization process. Fig. 4c demonstrates the relationship between μ_e and B_s relative to Nb content. μ_e exhibits an initial increase, reaching a peak at 2 at.% Nb, after which it declines. Conversely, B_s decreases monotonically as Nb content increases. Notably, the alloy containing 2 at.% Nb showcases significant GFA and superior comprehensive soft magnetic properties, thus leading to the subsequent preparation of the alloy powder *via* gas atomization.

Fig. 4d presents the surface morphology of the gas-atomized $Fe_{73.3}P_5Si_{7.6}B_{9.5}C_{1.9}Nb_2Cu_{0.7}$ amorphous powder. Most of the magnetic powder particles exhibit a smooth surface and high sphericity, which enhance the coating's integrity and uniformity, thereby reducing eddy current losses between particles [8,30]. Fig. 4e illustrates the particle size distribution of original powders with D_{50} and D_{90} are 30.9 and 40.3 μm, respectively. Fig. 4f shows the XRD patterns of the original powder with different particle sizes. For powders in the 0–75 μm size range, only a broad diffuse scattering peak is observed, indicating a fully amorphous structure. In contrast, powders in the 75–125 μm size range

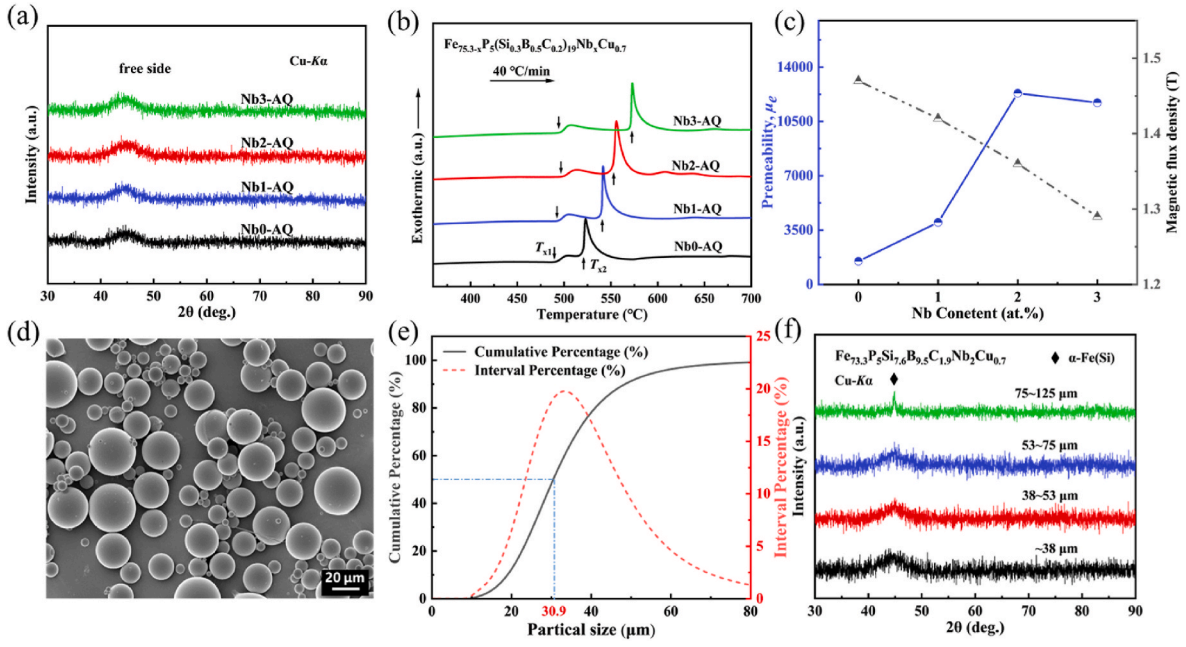

Fig. 4. (a) XRD patterns, (b) DSC curves and (c) permeability and magnetic flux density of as-cast $Fe_{75.3-x}P_5Si_{7.6}B_{9.5}C_{1.9}Cu_{0.7}Nb_x$ (x = 0, 1, 2 and 3) alloy ribbons; (d) SEM morphology, (e) particle size distribution and (f) XRD patterns of gas-atomized $Fe_{73.3}P_5Si_{7.6}B_{9.5}C_{1.9}Nb_2Cu_{0.7}$ amorphous powders.

exhibit a small crystallization peak corresponding to the α-Fe(Si) phase near 2θ = 44.5°. Analysis of the particle size distribution confirms that 83 % of the powders (particle size <75 μm) are fully amorphous, highlighting the strong glass-forming ability of the alloy composition. Furthermore, particle size significantly influences not only the amorphous fraction but also the soft magnetic properties, including eddy current loss and magnetic permeability. Based on a comprehensive evaluation of amorphous powder yield and soft magnetic performance, fully amorphous alloy powders in the 0–54 μm size range were selected to prepare SMCs.

3.3. Characterization of the insulation layer

Apart from the composition of the powder, the component, structure and thickness of the insulation layer can significantly affect the high-frequency performance of the SMCs. A series of experimental validations were conducted to uncover the underlying mechanisms and contributing factors. Fig. 5 reveals the evolution of surface morphologies and the EDS measurement of the oxygen (O) elemental mass fraction of AMPC and AMPO-n. The AMPC exhibits a smooth and pristine surface with only 3.79 % oxygen content. In contrast, after treatment with HNO_3, AMPO-n surfaces exhibit pronounced roughening, accompanied by a significant increase in the O oxygen content, confirming the formation of an oxide layer. The presence of an oxidized layer is certified to enhance the electrical resistivity [31], thereby mitigating eddy current losses between individual powder particles. Notably, the oxide layer of AMPO-5 is relatively porous and loosely structured, characterized by a uniform micro-pore distribution (Fig. 5d). Conversely, AMPO-10 and AMPO-20 exhibit a more compact, continuous thicker oxide layer (Fig. 5f–h). FTIR was performed on the powder particles further to elucidate the composition of the surface oxide layer. The strong absorption bands at 3440 cm^{-1} and 1630 cm^{-1} correspond to the stretching vibration of -OH bonds, indicative of water absorbed on the powder surface (Fig. 6). Additionally, the absorption band at 1060 cm^{-1} is attributed to the Si-O-Si stretching vibration absorption band [32]. Notably, the FTIR spectra of the AMPC for comparison exhibit similar characteristic absorption features, albeit with lower intensity, which can be ascribed to mild surface oxidation resulting from gas atomization in a relatively low vacuum environment. Following HNO_3 oxidation, a new absorption band near 1380 cm^{-1} emerges, corresponding to Fe-OH vibration absorption modes, which become intense as the concentration of HNO_3 increases. The bands at 880 cm^{-1} and 800 cm^{-1} are associated with Fe-O vibration absorption [33,34]. Notably, a significant

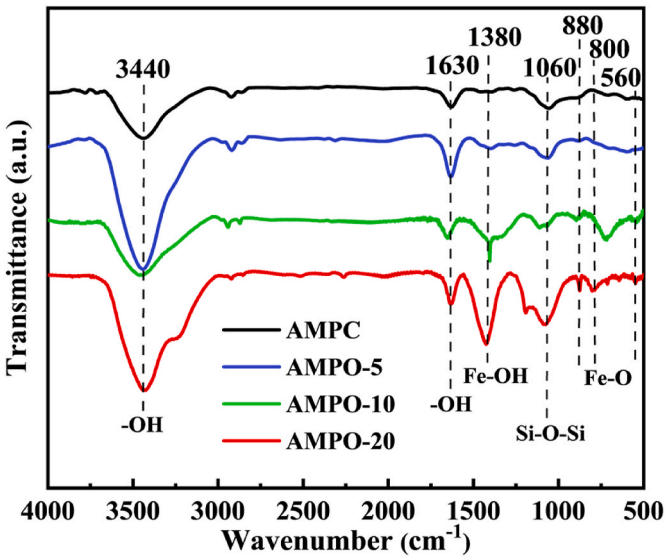

Fig. 6. FTIR spectra of AMPC and AMPO-n.

absorption band at 560 cm^{-1} in AMPO-10 and AMPO-20 is the characteristic of Fe_3O_4 [18,35]. This suggests the formation of Fe_3O_4 on the powder surface after HNO_3 treatment at concentrations of 10 wt% or higher. The shifting position and varying intensity of these characteristic absorption peaks with increasing HNO_3 concentration indicate an enhanced formation of Fe oxides and a corresponding evolution in the composition of the oxide layer.

XPS characterization was performed to investigate the surface chemistry of AMPO-n. As illustrated in Fig. 7a, the Fe 2p spectrum for AMPO-5 reveals distinct peaks corresponding to Fe^0 (707.2 eV), Fe^{2+} (709.9 eV) and Fe^{3+} (711.7 eV), along with characteristic satellite peaks at 719.9 and 731.9 eV, corroborating previous reports [36–38]. The relative abundance of Fe^{2+} and Fe^{3+} species yields a Fe^{2+}/Fe^{3+} ratio of approximately 4.05:1, aligning with stoichiometry of Fe_2O_3. The accompanying Si 2p spectrum (Fig. 7b) displays peaks at 98.6 eV and 102.4 eV, assigned to Si^0 and Si^{4+}, corresponding to elemental Si and SiO_2, respectively [39,40]. The simultaneous detection of Fe^0 and Si^0 indicates the formation of a thin insulating layer, possibly hindering complete oxidation [17]. The O 1s spectrum in Fig. 7c deconvoluted into four distinct peaks at 528.9, 530.0, 531.2 and 532.5 eV, attributed to

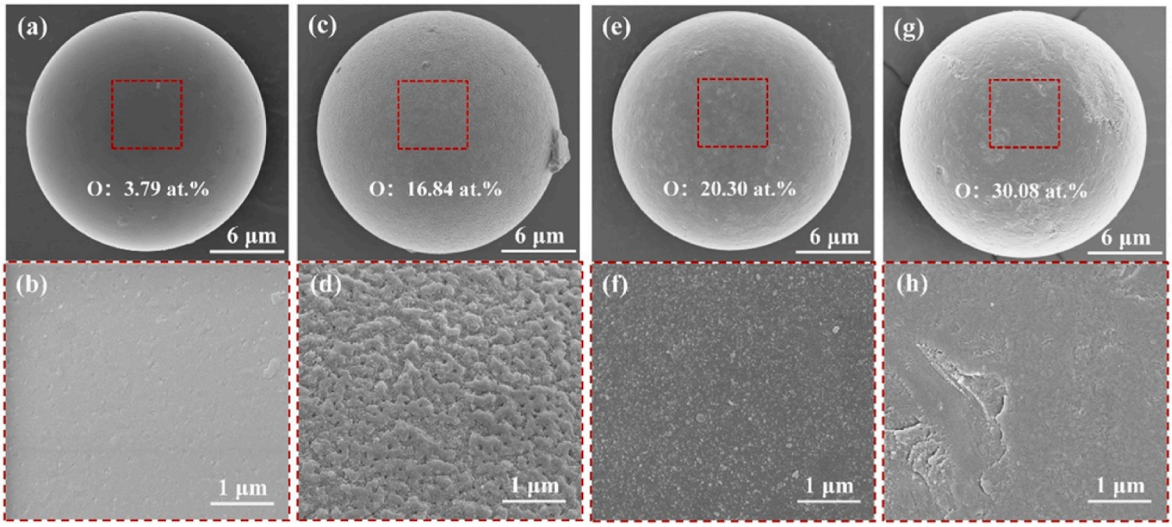

Fig. 5. SEM images depicting the surface morphology of (a) AMPC, (c) AMPO-5, (e) AMPO-10 and (g) AMPO-20; (b), (d), (f) and (h) are magnification for (a), (c), (e) and (g), respectively.

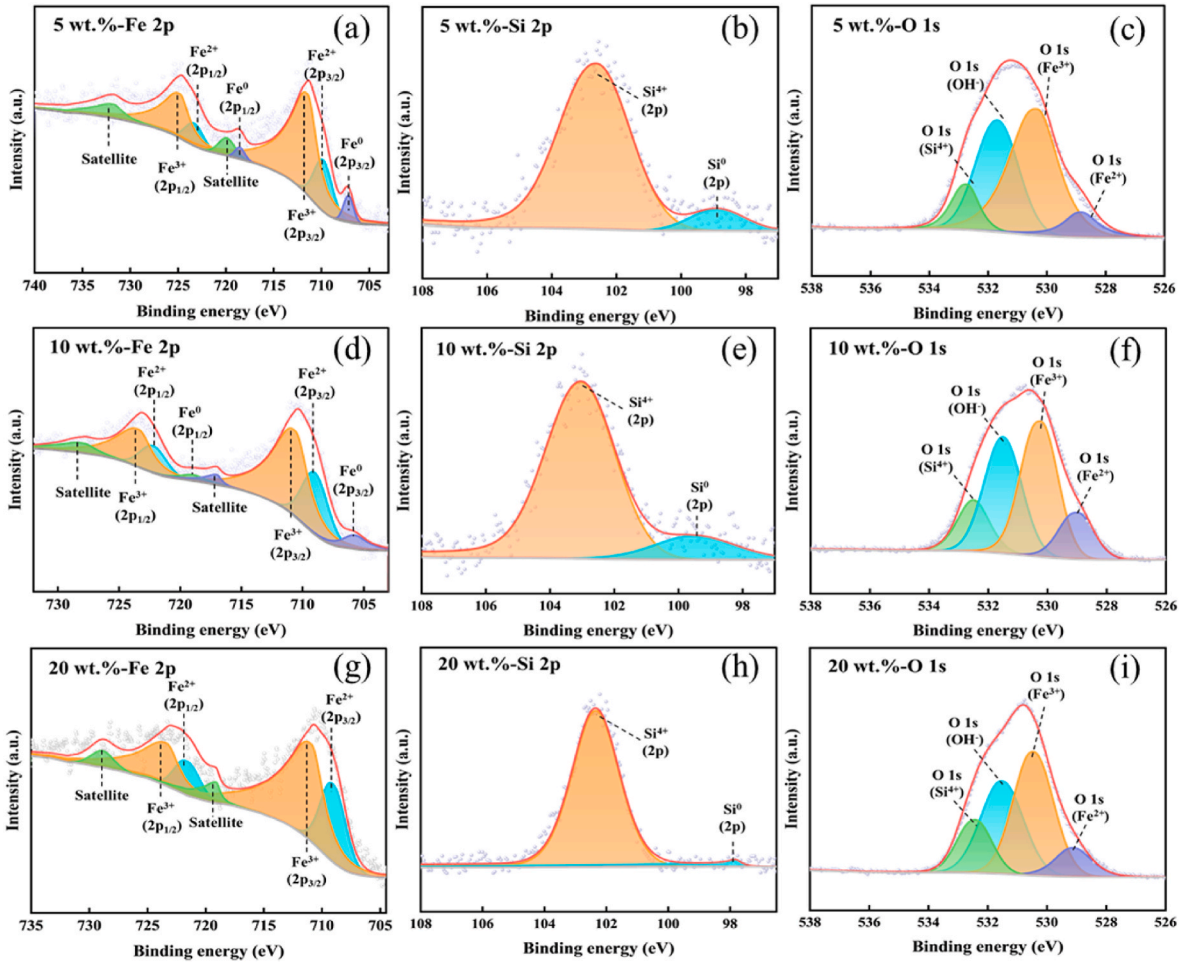

Fig. 7. XPS spectra of the (a, d, g) Fe 2p, (b, e, h) Si 2p, (c, f, i) O 1s core-level peaks recorded from powders of (a–c) AMPO-5, (d–f) AMPO-10, and (g–i) AMPO-20.

Fe^{2+}, Fe^{3+}, OH^-, and Si^{4+} [40–42], respectively. These results suggest that the surface layer of AMPO-5 primarily comprises Fe_2O_3, SiO_2, and hydroxides. As the HNO_3 concentration increases to 10 wt%, the Fe 2p spectrum (Fig. 7d) exhibits peaks at 705.8 eV, 709.1 eV and 710.9 eV, corresponding to Fe^0, Fe^{2+}, and Fe^{3+}, respectively. The Fe^{2+}/Fe^{3+} ratio, now approaching 1:2, is consistent with the presence of Fe_3O_4. In parallel, the Si 2p spectrum reveals the persistence of Si^0 and Si^{4+} states (Fig. 7e), whereas the O 1s spectrum retains contributions from Fe^{2+}, Fe^{3+}, OH^-, and Si^{4+} species (Fig. 7f). This analysis suggests that the oxide layer formed at AMPO-10 mainly comprises Fe_3O_4, SiO_2, and hydroxides. With the HNO_3 concentration increased to 20 wt%, the Fe 2p spectrum demonstrates a significant attenuation of the Fe^0 signal, indicative of a thicker insulating layer formed (Fig. 7g). The spectral profile highlights the dominance of Fe^{3+} and Fe^{2+} states alongside the persistence of satellite peaks. Notably, the Fe^{2+}/Fe^{3+} ratio falls below 1:2, suggesting the coexistence of Fe_2O_3 and Fe_3O_4. The Si 2p spectrum

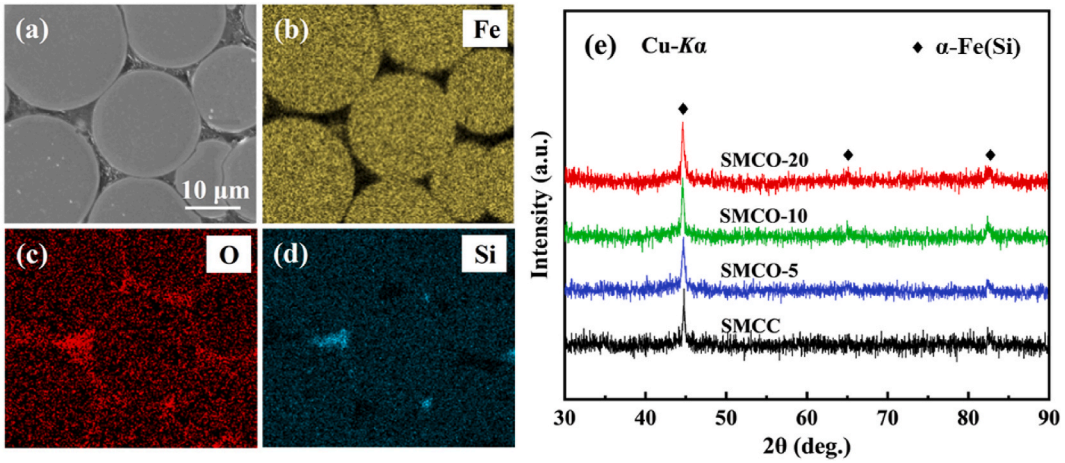

Fig. 8. (a–d) Cross-sectional SEM images of SMCO-20, accompanied by corresponding EDS mappings, (e) XRD patterns of SMCC and SMCO-n after annealing treatment.

shows both Si^0 and Si^{4+} contributions, although the Si^0 peak area diminishes considerably, implying enhanced oxidation (Fig. 7h). O 1s spectrum maintains peaks corresponding to Fe^{2+}, Fe^{3+}, OH^-, and Si^{4+}, consistent with prior observations (Fig. 7i). Consequently, the oxide layer of AMPO-20 predominantly contains Fe_2O_3, Fe_3O_4, SiO_2 and hydroxides.

To investigate whether the annealing treatment, pressure and EP coupling can affect the performance of AMPO-20 or not, the cross-sectional morphology, elements mapping and phase constituent of SMCO-20 are shown in Fig. 8. The surface of the powder is covered with a complete layer of insulating EP and the homogeneous distribution of O elements between the powder particles, indicating the formation of a uniform oxide layer throughout SMCO-20 (Fig. 8c). Moreover, under the cold pressing condition of 1800 MPa, the powder exhibits no plastic deformation, retaining its high sphericity, which is indicative of the significant mechanical strength of AMPO-20. Additionally, the XRD patterns of SMCC and SMCO-n annealed at 480 °C show no detectable diffraction peaks other than those corresponding to the α-Fe(Si) phase, suggesting that the oxide layer during oxidation is too thin to be detected by XRD (Fig. 8e).

Details of oxidation layers of SMCO-10 and SMCO-20 were further investigated through cross-sectional TEM, as shown in Fig. 9. The oxidation layer is observed as a distinct grey region situated above the Fe-based magnetic powder matrix, indicating the formation of a uniform and compact coating that adheres well to the substrate (Fig. 9a, c). The thickness of the oxidation layer varies with the concentration of HNO_3, with approximately 20 nm for AMPO-10 and 74 nm for AMPO-20. This structural integrity ensures the creation of an effective barrier, preventing direct contact between individual powder particles. The TEM images and corresponding EDS elemental mappings presented in Fig. 9b, d further elucidate the chemical composition of the oxidation layer. The EDS analysis confirms the presence of Fe, O, and Si, indicating that the oxidation layer predominantly consists of iron oxides and silicon oxides. Notably, the transition in the oxide layer composition and thickness plays a pivotal role in improving insulation. A thicker oxidation layer ensures superior electrical isolation, minimizing eddy current losses while preserving the magnetic properties critical for high-frequency applications.

Grain size distribution measurements and SAED analysis were conducted to investigate further the impact of annealing treatment on the structural characteristics of SMCO-10 and SMCO-20. The uniform dispersion of small α-Fe(Si) nanocrystals within the amorphous matrix plays a critical role in the soft magnetic properties of these materials. The exchange interaction between grains effectively averages out the local magnetocrystalline anisotropy, enhancing the magnetic performance [43,44]. Fig. 10a, c reveals that fine α-Fe(Si) nanograins are uniformly and randomly distributed within the amorphous matrix in both samples. The diffraction rings corresponding to the (110), (200), and (211) planes confirm the presence of nanocrystalline α-Fe(Si) phases, demonstrating a consistent crystalline structure across oxidation conditions. The grain size distributions show minimal variation in response to the HNO_3 concentration. For SMCO-10, the average grain size was 14.4 nm, while a slight reduction to 14.1 nm was observed in SMCO-20. This negligible change in grain size indicates that the HNO_3 oxidation process exerts little influence on the internal crystalline structure. These findings demonstrated that the primary effect of HNO_3 oxidation lies in the formation and growth of the surface oxide layer rather than altering the internal nanograin structure of the powder.

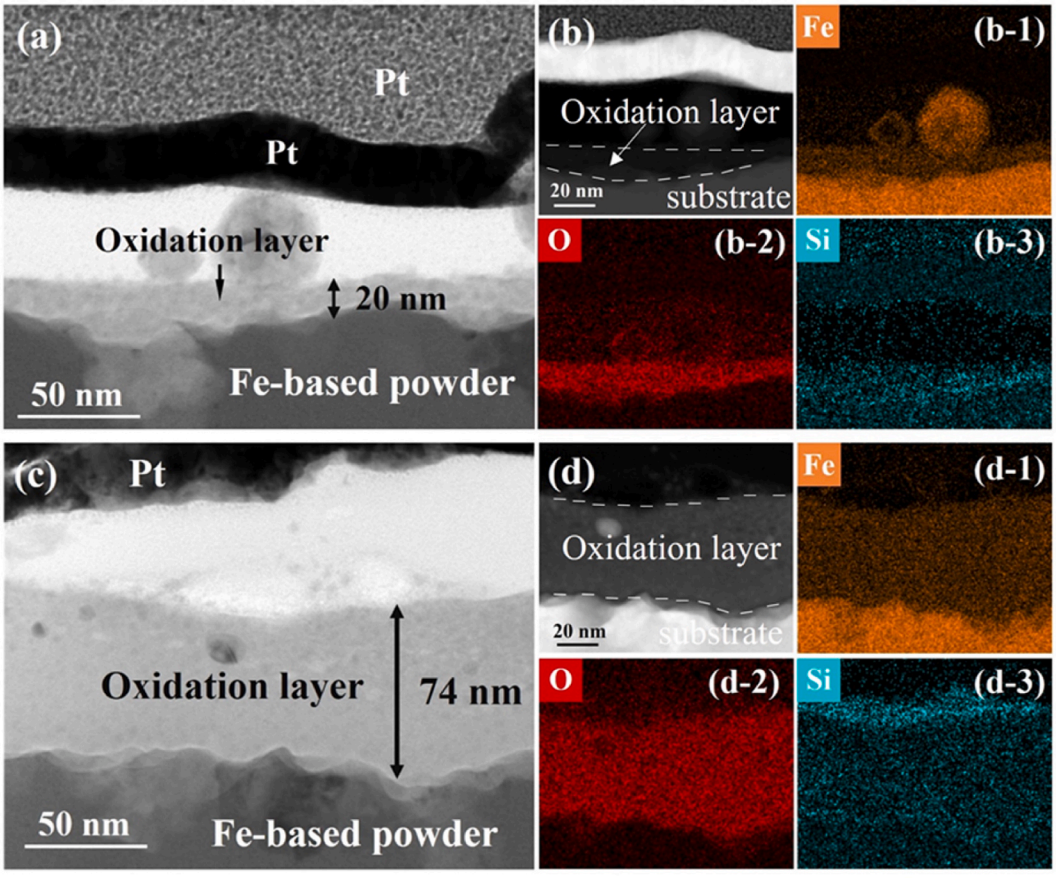

Fig. 9. Cross-sectional TEM analysis of oxidation layers formed on (a, b) SMCO-10 and (c, d) SMCO-20; (b, d) TEM images with corresponding EDS elemental maps for Fe (b-1, d-1), O (b-2, d-2), and Si (b-3, d-3).

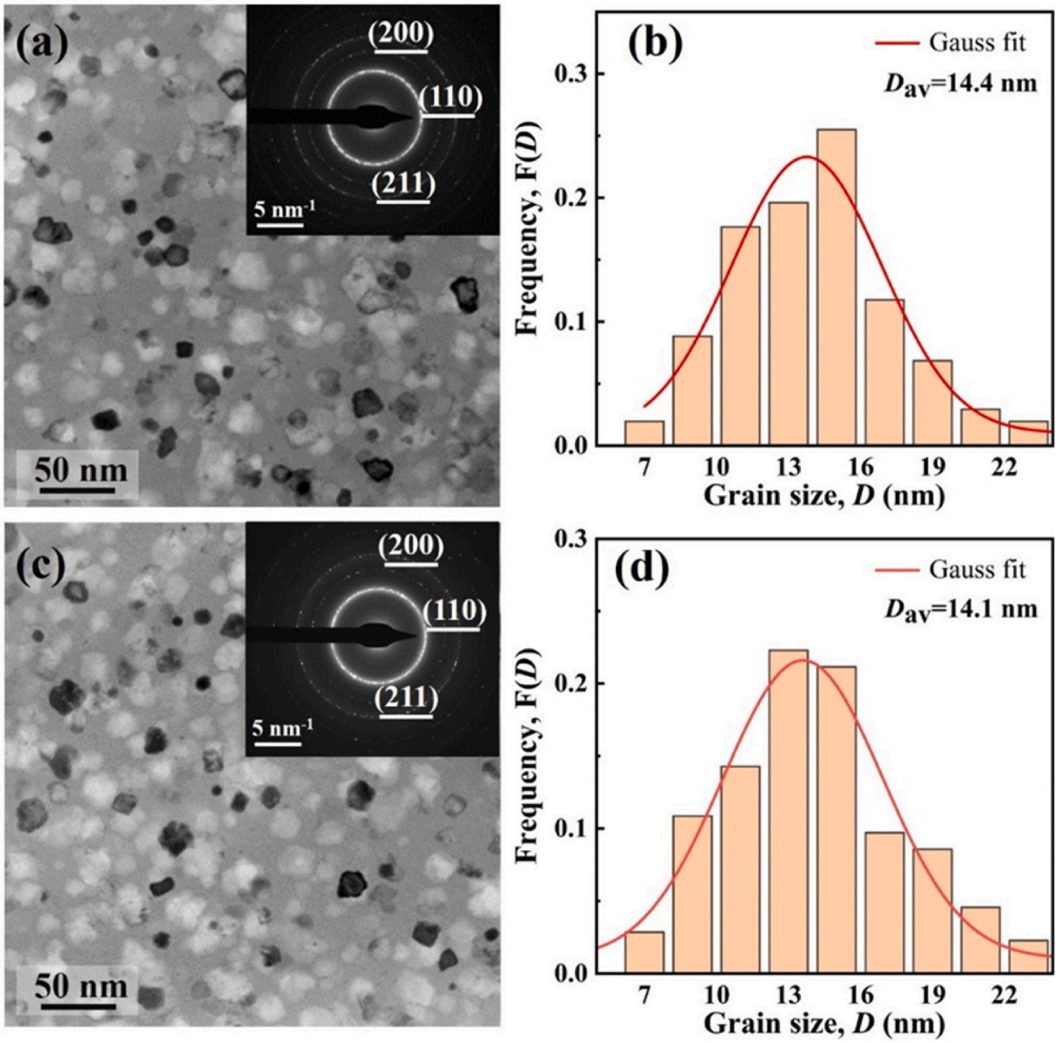

Fig. 10. (a) TEM micrograph and (b) corresponding grain size distribution of AMPO-10, (c) TEM micrograph and (d) grain size distribution of AMPO-20.

3.4. Growth mechanism of insulation layers for SMCO-n

The growth mechanism of the oxidation layer *via* in situ HNO_3 oxidation can be inferred from the preceding analysis and is schematically illustrated in Fig. 11. The oxidation process yields a bilayer-structured coating on the AMPC, comprising an inner barrier layer and an outer precipitation layer consistent with previously reported passivation models [45]. During the initial stages of passivation, Fe and Si atoms at the powder surface are directly oxidized into SiO_2, Fe_3O_4 and Fe_2O_3, forming a compact inner oxide layer. As oxidation proceeds, Fe and Si atoms further dissolve, releasing cations such as Fe^{3+}, which diffuse through the barrier layer to accumulate at the interface between the barrier layer and the surrounding HNO_3 solution. This migration of Fe^{3+} reduces the local concentration of H^+ ions near the powder surface, thereby increasing the pH. As a result, transient precipitation of hydroxides, such as $Fe(OH)_3$, occurs, temporarily blocking the powder surface and contributing to the formation of the outer precipitation layer. However, the presence of H^+ ions in the HNO_3 solution also facilitates the dissolution of these hydroxides, creating a dynamic equilibrium between hydroxide precipitation and dissolution. This cyclical process governs the growth of the outer layer. The barrier layer consists primarily of Fe oxides (Fe_2O_3, Fe_3O_4) and SiO_2, while the precipitation layer is composed of $Fe(OH)_3$. The formation of these layers reflects the complex interplay between ion migration, precipitation, and

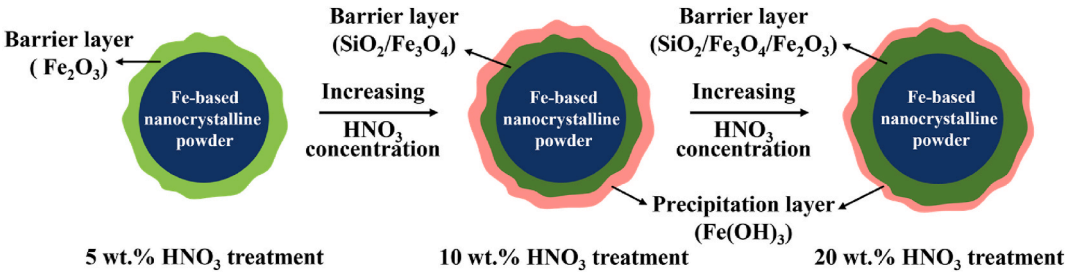

Fig. 11. Schematic of insulation layer growth on the surface powder.

dissolution, all of which influence the final oxide structure. Thermodynamically, both Fe and Si in the powder can be oxidized by HNO_3 as indicated by the following reactions, where the negative changes in the Gibbs free energy ($\Delta_r G_m^\theta$) demonstrate the spontaneous nature of the oxidation process [46]:

$$2Fe + 6HNO_3(\text{dilute}) = Fe_2O_3 + 6NO + 3H_20 \quad \Delta_r G_m^\theta = -1140.95\ kJ/mol \tag{1}$$

$$3Fe + 8HNO_3 = Fe_3O_4 + 8NO_2 + 4H_20 \quad \Delta_r G_m^\theta = -907.96\ kJ/mol \tag{2}$$

$$2Fe_3O_4 + 2HNO_3 = 3Fe_2O_3 + 2NO_2 + H_20 \quad \Delta_r G_m^\theta = -168.94\ kJ/mol \tag{3}$$

$$3Si + 3NO_3^- + 4H^+ = 3SiO_2 + 4NO + 2H_20 \quad \Delta_r G_m^\theta = -387.26 kJ/mol \tag{4}$$

At low concentration of 5 wt% HNO_3, the powder surface is not sufficiently passivated, resulting in direct oxidation into Fe_2O_3 following reaction (1). At 10 wt% HNO_3, passivation occurs through forming Fe_3O_4 (reaction (2)), generating a relatively dense and stable barrier layer with limited thickness. When the HNO_3 concentration is increased to 20 wt%, a thicker passivation layer forms due to accelerated oxidation. Over time, part of the Fe_3O_4 in the barrier layer is further oxidized into the thermodynamically more stable Fe_2O_3 (reaction (3)). Thus, the oxidation behaviour of the Fe-based powders is governed by the interplay between passivation, ion migration, and hydroxide precipitation, with the varying concentration of HNO_3 playing a pivotal role in determining the final composition and structure of the insulation layer. The morphology and uniformity of the oxidation layer, in turn, have profound implications for the magnetic properties of the composite material.

3.5. Correlating the growth of the insulation layer with the performance of SMCO-n

Analysis on the detailed growth of the insulation layers allows insights into the performance of SMCs. Permeability change is attributable to the formation of the oxidation layer. For SMCO-10 and SMCO-20, a compact and uniform oxidation layer minimizes demagnetizing fields, enhancing permeability (Fig.s. 2a and 5f–h) [47]. In contrast, a porous and less effective Fe_2O_3 coating leads to poor permeability (Figs. 2a, Fig 5d). Ferrimagnetic Fe_3O_4 can reduce magnetic dilution, while Fe_2O_3 provides both electrical and magnetic insulation for powder particles. The synergistic effect of Fe_3O_4 and Fe_2O_3 not only enhances permeability but also improves the cut-off frequency. Additionally, compared to SMCO-10, SMCO-20 has a thicker insulating layer and introduces a larger demagnetization field, further improving the cut-off frequency. (Fig.s. 2b–Figs. 5–7, Fig 9). Insulation layer also contributes to the improvement DC-bias of SMCO-n by introducing a higher demagnetization field and reducing the effective magnetic field within individual particles. By mitigating premature saturation, SMCO-n demonstrates superior DC-bias performance than SMCC, enhancing their suitability for operation under high-current conditions (Figs. 2c, Fig 9) [48]. The loss separation analysis has been conducted to elucidate the mechanism underlying the effect of the insulation layer on the P_{cv}. Theoretically, P_{cv} can be decomposed into P_h, P_e and P_{exc}, as described by Bertotti's classic theory [49] and Kollar's theory [50]. The loss model can be expressed as:

$$P_{cv} = P_h + P_e + P_{exc} \tag{5}$$

$$P_{cv} = C_h B_m^\alpha f + C_e B_m^2 f^2 + C_{exc} B_m^x f^y \tag{6}$$

Where C_h, C_e and C_{exc} represent the hysteresis loss coef ficient, eddy current, and excess loss coefficient, respectively, f is the frequency.

The variation in P_h after loss separation is displayed in Fig. 12a. The SMCO-n exhibit higher hysteresis losses compared to SMCC, primarily due to the influence of the oxidation layer. The presence of ferrimagnetic or non-magnetic phases within the oxide layer impedes domain wall motion, thus reducing exchange coupling between powder particles and increasing P_h [20,51]. The SMCO-5 shows the highest P_h, which can be attributed to the predominance of Fe_2O_3, a non-magnetic phase that more effectively hinders domain wall motion than Fe_3O_4 [20]. As the concentration of HNO_3 increases from 10 wt% to 20 wt%, the oxide layer thickens, leading to an enhanced demagnetization field and a subsequent increase in hysteresis loss [22]. P_e arises from the eddy currents in response to alternating magnetic fields applied on soft magnetic materials [49,52,53]. Normally, P_e can be divided into inter-particle (P_e^{inter}) and intra-particle (P_e^{intra}) components [21,27]. The P_e^{inter} originates from the eddy current circulating among the particles in the entire SMCs, often caused by non-uniform coating or damage to the insulation layer during compaction. In contrast, P_e^{intra} arises from eddy current within individual magnetic particles. Then, P_e^{inter} and P_e^{intra} can be expressed as:

$$P_e^{inter} = \frac{(\pi d_e)^2}{\rho_s \beta_1} B_m^2 f^2 \tag{7}$$

$$\beta_1 = \frac{6}{1 - 0.633(w/h)\tanh(1.58h/w)} \tag{8}$$

$$P_e^{intra} = \frac{(\pi d_p)^2}{20\rho_p} B_m^2 f^2 \tag{9}$$

Where d_e is the effective eddy current dimension (the shorter edge of the core's rectangular cross-section), β_1 is a geometric factor related to the core cross-section, ρ_s is the electrical resistivity of the composite. Where d_p is the particle diameter, and ρ_p is the electrical resistivity of the magnetic particles.

The variation of P_e^{inter} and P_e^{intra} under the condition of $B_m = 0.05$ T is illustrated in Fig. 12b. The P_e^{intra}, calculated from equation (9), shows no notable variation across the samples due to the similar AMPC size distribution used for all SMCs in this study. However, P_e^{inter} exhibits great change amongst different samples. Compared to SMCC, SMCO-5 shows only a slight reduction in P_e^{inter}, indicating that the porous and less effective Fe_2O_3 layer provides insufficient insulation. Conversely, SMCO-10 and SMCO-20 exhibit a significant reduction in P_e^{inter}, underscoring the enhanced insulating performance of their dense oxide layers by increasing ρ_s. SMCO-20 shows a lower value than SMCO-10, attributed to the formation of a thicker oxidation layer (Figs. 6–7, Fig 9). When SMCs are applied under high frequency, P_{exc} becomes a severe issue [54]. It has been reported the P_{exc} of $Fe_{73.5}Si_{15.5}B_7Cu_1Nb_3$ nanocrystalline can reach 88 kW/m^3 (100 mT, 200 kHz), which accounts for 90 % of the core loss [3]. The large percent of P_{exc} in total P_{cv} becomes an urgent problem for improving SMCs performance. As is shown in Fig. 12d, P_{exc} contributes relatively little to the total loss under low and medium frequencies. However, as the frequency increases, the proportion of P_{exc} rises, accounting only 50 % of the total loss at 1 MHz, which suggests the in-situ insulation layer significantly decline the proportion of P_{exc}. Besides, the dense oxide insulation also improves the P_{exc} at higher frequencies, which can be attributed to the shift in the cut-off frequency toward higher values [55]. Thus, in the SMCO-n, the insulation layer exhibits a consistent impact on P_h, P_e and P_{exc} by adjusting the concentration of HNO_3. P_h, P_{exc} and P_e^{inter} can be reduced simultaneously. These findings indicate that HNO_3 treatment plays a critical role in modulating the morphology and uniformity of the oxidation layer, which may, in turn, have profound implications for the magnetic properties of the composite material.

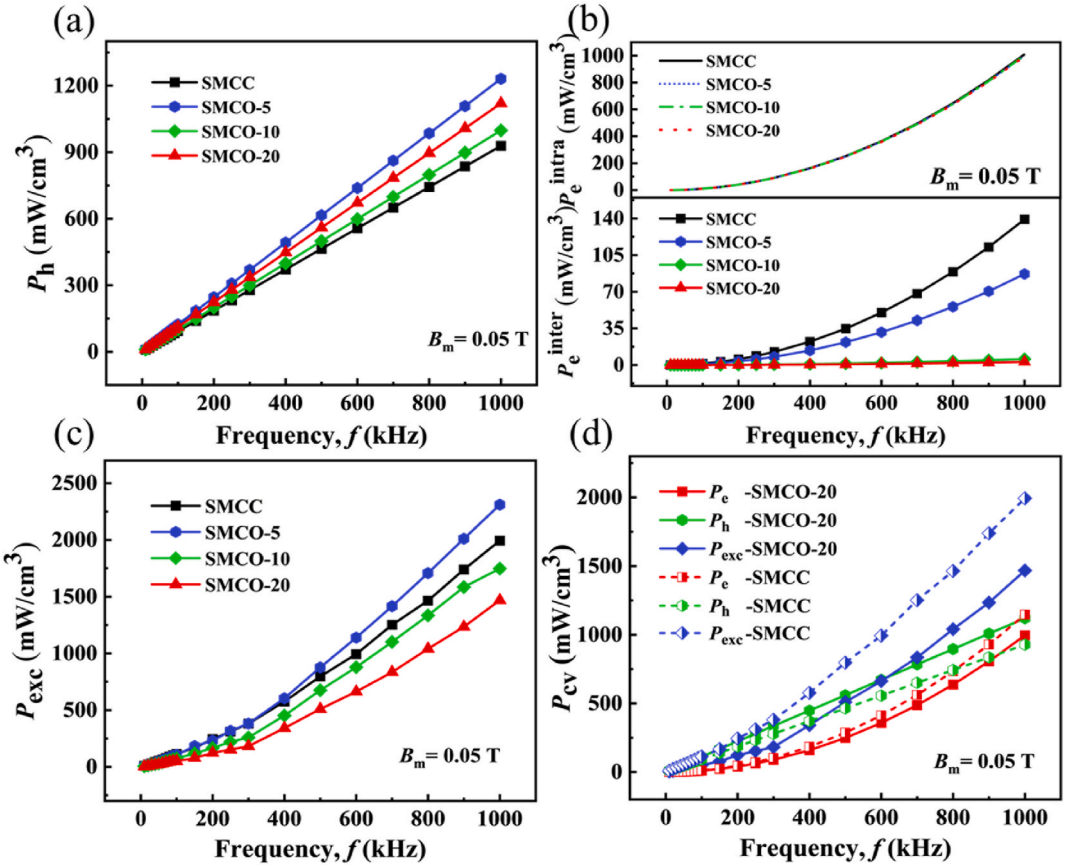

Fig. 12. (a) Power loss analysis of SMCC and SMCO-n as a function of the frequency: (a) P_h, (b) P_e^{intra} and P_e^{inter}, (c) P_{exc}; (d) the comparison of P_e, P_h and P_{exc} between SMCC and SMCO-20 (B_m = 0.05 T).

4. Conclusion

In this study, a novel FePSiBCNbCu nanocrystalline with comprehensive soft properties and high GFA was designed. The optimally designed $Fe_{73.3}P_5Si_{7.6}B_{9.5}C_{1.9}Nb_2Cu_{0.7}$ were successfully prepared by gas atomization with a fully amorphous structure. Afterwards, high-frequency soft magnetic properties of $Fe_{73.3}P_5Si_{7.6}B_{9.5}C_{1.9}Nb_2Cu_{0.7}$ nanocrystalline SMCs were successfully fabricated by introducing an insulation layer with HNO_3 oxidation treatment. The oxidation process, controlled by HNO_3 concentration, yields a bilayer oxide structure consisting of a dense barrier layer and a more porous outer precipitation layer. As the concentration of HNO_3 increases, a uniform and dense Fe_3O_4 oxide layer forms on the powder surface. This ferrimagnetic oxide layer not only acts as an insulator but also reduces the magnetic dilution effect, playing a key role in the observed improvements in magnetic properties. The densification of the oxide layer in samples with higher HNO_3 concentration (SMCO-10, SMCO-20) significantly reduces P_h, P_e, and P_{exc} reveals that the presence of a uniform and compact oxide layer is integral to reducing overall core loss. Moreover, the enhanced insulation layer improves the high-frequency response and mitigates P_{exc} at elevated frequencies, making the materials more suitable for high-current, high-frequency applications. SMCs demonstrated superior magnetic performance, including highly stable μ' remained between 30 and 47 up to 20 MHz, excellent DC-bias permeability increase from 57.8 % to 82.7 % under 100 Oe, high cut-off frequency up to 96 MHz, and low P_{cv} that regulated less than 153–173 mW/cm^3 (50 mT, 100 kHz), 590–663 mW/cm^3 (100 mT, 100 kHz). This study provides significant insights into the design of Fe-based soft magnetic composites with tailored insulation properties, enabling the optimization of their performance for advanced applications. The correlation between oxide layer characteristics and composite performance highlights the importance of controlling the oxidation process for future material design, ultimately leading to more efficient and reliable SMCs for next-generation electronic and energy systems.

CRediT authorship contribution statement

Zhijun Guo: Writing – review & editing, Methodology, Investigation. **Xingyu Zheng:** Writing – original draft, Methodology, Investigation. **Changlong Jin:** Data curation. **Yanzhou Fan:** Data curation. **Mingjuan Cai:** Methodology. **Jifeng Zhou:** Investigation. **Wanying Dong:** Data curation. **Qiang Luo:** Conceptualization. **Baolong Shen:** Supervision, Resources, Conceptualization, Funding acquisition.

Declaration of competing interest

The authors declare that they have no known competing financial interests or personal relationships that could have appeared to influence the work reported in this paper.

Acknowledgements

This work was financially supported by the National Key R&D Program of China (No. 2022YFB3804100), the National Natural Science Foundation of China (No. 52231005), the Jiangsu Provincial Key R&D Program, China (No. BE2021088), and the Start-up Research Fund of Southeast University, China (No. RF1028623113), Open Research Fund of Jiangsu Key Laboratory of Advanced Metallic Materials, Southeast University, China (No. AMM2025A01, AMM2024A02, AMM2023B05), the Science Technology Development Program of Yixing, China (No. C2024002).

Data availability

Data will be made available on request.

References

[1] J.Y. He, H. Yuan, M. Nie, H. Guo, H.Y. Yu, Z.W. Liu, R. Sun, Soft magnetic materials for power inductors: state of art and future development, Mater. Today Electron. 6 (2023) 100066.

[2] X.L. Peng, A. Zhang, J. Li, S.Y. Yu, J.S. Chang, M.H. Ge, Y.T. Yang, J.C. Xu, B. Hong, D.F. Jin, H.X. Jin, X.Q. Wang, H.L. Ge, J.F. Fang, Design and fabrication of Fe–Si–Al soft magnetic composites by controlling orientation of particles in a magnetic field: anisotropy of structures, electrical and magnetic properties, J. Mater. Sci. 54 (11) (2019) 8719–8726.

[3] E.A. Périgo, B. Weidenfeller, P. Kollár, J. Füzer, Past, present, and future of soft magnetic composites, Appl. Phys. Rev. 5 (3) (2018) 031301.

[4] S.H. Lu, M.G. Wang, Z.K. Zhao, Recent advances and future developments in Fe-based amorphous soft magnetic composites, J. Non-Cryst. Solids 616 (2023) 122440.

[5] G. Ma, L. Cheng, L.C. Lu, F.Y. Yang, X. Chen, C.Z. Zhu, Effects of DC bias on magnetic performance of high grades grain-oriented silicon steels, J. Magn. Magn Mater. 426 (2017) 575–579.

[6] M. Yan, X.L. Peng, Fundamentals of Magnetics and Magnetic Materials, second ed., Zhejiang University Press, Hang zhou, 2019.

[7] O. Gutfleisch, M.A. Willard, E. Bruck, C.H. Chen, S.G. Sankar, J.P. Liu, Magnetic materials and devices for the 21st century: stronger, lighter, and more energy efficient, Adv. Mater. 23 (7) (2011) 821–842.

[8] X.B. Li, Y.Q. Dong, X.C. Liu, S.D. Wu, R.L. Zhao, H. Wu, W. Gao, A.N. He, J.W. Li, X. M. Wang, Structure evolution of Fe-based nanocrystalline soft magnetic powder cores with excellent properties, Mater. Sci. Eng. B 285 (2022) 115965.

[9] H. Shokrollahi, K. Janghorban, Different annealing treatments for improvement of magnetic and electrical properties of soft magnetic composites, J. Magn. Magn Mater. 317 (1–2) (2007) 61–67.

[10] L.Y. Xing, Y.Q. Dong, X. Li, X.J. Jia, L. Zhang, A.N. He, J.W. Li, Q.K. Man, B. G. Shen, Significant improving magnetic properties and thermal conductivity of FeBSiPCNbCu nanocrystalline powder cores by designing novel ZnO insulating layer, J. Mater. Res. Technol. 33 (2024) 3358–3366.

[11] J.Y. Zhang, Y.Q. Dong, Y.Q. Li, L.P. Yang, X.J. Jia, L. Zhang, L.W. Cai, A.N. He, J. W. Li, X.C. Liu, B.G. Shen, The effect of phosphate/TiO_2 composite insulating layer on the high frequency magnetic properties of FeSiBPCNbCu nanocrystalline soft magnetic powder cores, Mater. Today Commun. 38 (2024) 107809.

[12] Y. Yoshizawa, S. Oguma, K. Yamauchi, New Fe-based soft magnetic alloys composed of ultrafine grain structure, J. Appl. Phys. 64 (10) (1988) 6044–6046.

[13] T. Takahashi, K. Yoshida, Y. Shimizu, A.D. Setyawan, M. Bito, M. Abe, A. Makino, Fe-Si-B-P-C-Cu nanocrystalline soft magnetic powders with high Bs and low core loss, AIP Adv. 7 (5) (2017) 056111.

[14] H. Li, A.D. Wang, T. Liu, P.B. Chen, A.N. He, Q. Li, J.H. Luan, C.-T. Liu, Design of Fe-based nanocrystalline alloys with superior magnetization and manufacturability, Mater. Today 42 (2021) 49–56.

[15] B. Zhou, Y.Q. Dong, Q. Chi, Y.Q. Zhang, L. Chang, M.J. Gong, J.J. Huang, Y. Pan, X. M. Wang, Fe-based amorphous soft magnetic composites with SiO_2 insulation coatings: a study on coatings thickness, microstructure and magnetic properties, Ceram. Int. 46 (9) (2020) 13449–13459.

[16] S. Nakahara, E.A. Périgo, Y. Pittini-Yamada, Y. de Hazan, T. Graule, Electric insulation of a FeSiBC soft magnetic amorphous powder by a wet chemical method: identification of the oxide layer and its thickness control, Acta Mater. 58 (17) (2010) 5695–5703.

[17] M. Yan, Q.M. Chen, D. Liu, C. Wu, J. Wang, Sodium nitrate passivation as a novel insulation technology for soft magnetic composites, Engineering 20 (2023) 134–142.

[18] A.M. Jubb, H.C. Allen, Vibrational spectroscopic characterization of hematite, maghemite, and magnetite thin films produced by vapor deposition, ACS Appl. Mater. Interfaces 2 (10) (2010) 2804–2812.

[19] G.L. Zhao, C. Wu, M. Yan, Enhanced magnetic properties of Fe soft magnetic composites by surface oxidation, J. Magn. Magn Mater. 399 (2016) 51–57.

[20] Y.D. Wu, Z. Dong, N.N. Shen, Y.L. Li, S. Zhang, F.S. Li, Y.Q. Dong, X.D. Hui, Magnetic properties of an Fe-based amorphous soft magnetic composite prepared via in-situ steam oxidation, Intermetallics 166 (2024) 108174.

[21] W.J. Li, W.C. Li, J.K. Wu, X.F. Han, Y. Ying, J. Yu, J.W. Zheng, L. Qiao, J. Li, S. L. Che, Particles size-dependent magnetic properties of a FeSiAl soft magnetic composite with hybrid insulating coating for MHz applications, Mater. Sci. Eng. B 291 (2023) 116387.

[22] X.Y. Shi, X.Y. Chen, K. Wan, B.W. Zhang, P.T. Duan, H. Zhang, X.D. Zeng, W. Liu, H.L. Su, Z.Q. Zou, Y.W. Du, Enhanced magnetic and mechanical properties of gas atomized Fe-Si-Al soft magnetic composites through adhesive insulation, J. Magn. Magn Mater. 534 (2021) 168040.

[23] Z.L. Guo, J.H. Wang, W.H. Chen, D.C. Chen, H.B. Sun, Z.L. Xue, C. Wang, Crystal-like microstructural Finemet/FeSi compound powder core with excellent soft magnetic properties and its loss separation analysis, Mater. Des. 192 (2020) 108769.

[24] C. Kittel, On the theory of ferromagnetic resonance absorption, Phys. Rev. 73 (2) (1948) 155–161.

[25] W.C. Li, H.Q. Yan, Y. Ying, J. Yu, J.W. Zheng, L. Qiao, J. Li, S.L. Che, Analysis of the magnetic properties of a silicate-coated spherical FeSiAl-based soft magnetic composite for high-frequency power-applications, Appl. Phys. Lett. 115 (21) (2019) 212401.

[26] H. Shokrollahi, K. Janghorban, Soft magnetic composite materials (SMCs), J. Mater. Process. Technol. 189 (1–3) (2007) 1–12.

[27] W.C. Li, H.W. Cai, Y. Kang, Y. Ying, J. Yu, J.W. Zheng, L. Qiao, Y. Jiang, S.L. Che, High permeability and low loss bioinspired soft magnetic composites with nacre-like structure for high frequency applications, Acta Mater. 167 (2019) 267–274.

[28] J.J. Guo, Y.Q. Dong, Q.K. Man, Q. Li, C.T. Chang, X.M. Wang, R.W. Li, Fabrication of FeSiBPNb amorphous powder cores with high DC-bias and excellent soft magnetic properties, J. Magn. Magn Mater. 401 (2016) 432–435.

[29] C.T. Chang, Y.Q. Dong, M. Liu, H.Q. Guo, Q. Xiao, Y.F. Zhang, Low core loss combined with high permeability for Fe-based amorphous powder cores produced by gas atomization powders, J. Alloys Compd. 766 (2018) 959–963.

[30] S.D. Wu, Y.Q. Dong, R.L. Zhao, X.B. Li, H. Wu, W. Gao, A.N. He, J.W. Li, X.C. Liu, Microstructure evolution and soft magnetic property optimization of core-shell FeSiBCCr@SiO_2&ZrO_2 amorphous magnetic powder cores, Ceram. Int. 49 (5) (2023) 7515–7523.

[31] H. Cheng, X.H. Li, L.Y. Zhang, F.Y. Shen, X.G. Liu, Y.P. Sun, Ultra-low core loss FeSiAl soft magnetic composites with in-situ double oxidation layers of outer Fe_3O_4 layer and inner super-thin Al_2O_3/SiO_2 hybrid layer, Ceram. Int. 49 (16) (2023) 26568–26577.

[32] I. Halasz, M. Agarwal, R. Li, N. Miller, Vibrational spectra and dissociation of aqueous Na_2SiO_3 solutions, Catal. Lett. 117 (1–2) (2007) 34–42.

[33] S. Nasrazadani, The application of infrared spectroscopy to a study of phosphoric and tannic acids interactions with magnetite (Fe_3O_4), goethite (α-FeOOH) and lepidocrocite (γ-FeOOH), Corros. Sci. 39 (10–11) (1997) 1845–1859.

[34] M. Gotić, G. Dražić, S. Musić, Hydrothermal synthesis of α-Fe_2O_3 nanorings with the help of divalent metal cations, Mn^{2+}, Cu^{2+}, Zn^{2+} and Ni^{2+}, J. Mol. Struct. 993 (1–3) (2011) 167–176.

[35] Y.G. Zhao, J.X. Li, L.P. Zhao, S.W. Zhang, Y.S. Huang, X.L. Wu, X.K. Wang, Synthesis of amidoxime-functionalized Fe_3O_4@SiO_2 core–shell magnetic microspheres for highly efficient sorption of U(VI), Chem. Eng. J. 235 (2014) 275–283.

[36] F. Widdel, S. Schnell, S. Heising, A. Ehrenreich, B. Assmus, B. Schink, Ferrous iron oxidation by anoxygenic phototrophic bacteria, Nature 362 (6423) (1993) 834–836.

[37] H.B. Sun, Z.L. Guo, Z.K. Liang, W.H. Chen, Q.T. Zeng, C. Wang, Enhancements of preparation efficiency and magnetic properties for Fe-based amorphous magnetic flake powder cores upon the adoption of a novel double-paralleled slits nozzle, J. Magn. Magn Mater. 500 (2020) 166358.

[38] D.D. MacDonald, P. Butler, The thermodynamics of the aluminium—water system at elevated temperatures, Corros. Sci. 13 (4) (1973) 259–274.

[39] L.A. O'Hare, B. Parbhoo, S.R. Leadley, Development of a methodology for XPS curve-fitting of the Si 2p core level of siloxane materials, Surf. Interface Anal. 36 (10) (2004) 1427–1434.

[40] B. Hornetz, H.J. Michel, J. Halbritter, ARXPS studies of SiO_2-SiC interfaces and oxidation of 6H SiC single crystal Si-(001) and C-(001) surfaces, J. Mater. Res. 9 (12) (1994) 3088–3094.

[41] S. Wannaparhun, S. Seal, V. Desai, Surface chemistry of Nextel-720, alumina and Nextel-720/alumina ceramic matrix composite (CMC) using XPS–A tool for nano-spectroscopy, Appl. Surf. Sci. 185 (3) (2002) 183–196.

[42] T. Yamashita, P. Hayes, Analysis of XPS spectra of Fe^{2+} and Fe^{3+} ions in oxide materials, Appl. Surf. Sci. 254 (8) (2008) 2441–2449.

[43] M.J. Cai, Z.J. Guo, L. Li, X.Y. Zheng, X.X. Yang, Q.Q. Liu, G.P. Zou, B.L. Shen, Obtaining extremely low coercivity of high Bs FeCoBSiCPCu nanocrystalline alloys through modulation of magnetic anisotropy, J. Mater. Sci. Technol. 207 (2025) 105–112.

[44] M. Jiang, M. Cai, J. Zhou, S. Di, X. Li, Q. Luo, B. Shen, Superior high-frequency performances of Fe-based soft-magnetic nanocrystalline alloys, Mater. Today Nano 22 (2023) 100307.

[45] D.D. Macdonald, Passivity–the key to our metals-based civilization, Pure Appl. Chem. 71 (6) (1999) 951–978.

[46] J.A. Dean, Lange's Handbook of Chemistry, fifteenth ed., McGraw-Hill, Columbus, 1998.

[47] Q. Zhang, W. Zhang, K. Peng, In-situ synthesis and magnetic properties of core-shell structured Fe/Fe_3O_4 composites, J. Magn. Magn Mater. 484 (2019) 418–423.

[48] H.-I. Hsiang, L.-F. Fan, J.-J. Hung, Phosphoric acid addition effect on the microstructure and magnetic properties of iron-based soft magnetic composites, J. Magn. Magn Mater. 447 (2018) 1–8.

[49] G. Bertotti, General properties of power losses in soft ferromagnetic materials, IEEE Trans. Magn. 24 (1) (1988) 621–630.

[50] P. Kollár, Z. Birčáková, J. Füzer, R. Bureš, M. Fáberová, Power loss separation in Fe-based composite materials, J. Magn. Magn Mater. 327 (2013) 146–150.

[51] X.W. Tang, S.J. Zhu, R.H. Wei, L. Hu, J. Yang, W.H. Song, J.M. Dai, X.B. Zhu, Y. P. Sun, Exchange coupling and improved properties of the multilayer $CoFe_2O_4$/$La_{0.7}Sr_{0.3}MnO_3$ thin films, Compos. B Eng. 186 (2020) 107801.

[52] G.Y. Ouyang, B. Jensen, W. Tang, J. Schlagel, B. Hilliard, C.C. Pan, B.Z. Cui, K. Dennis, D. Jiles, T. Monson, I. Anderson, M.J. Kramer, J. Cui, Near net shape fabrication of anisotropic Fe-6.5%Si soft magnetic materials, Acta Mater. 201 (2020) 209–216.

[53] B.D. Cullity, C.D. Graham, Introduction to Magnetic Materials, second ed., John Wiley & Sons, Inc., Hoboken, 2009.
[54] H. Zhang, K. Wang, Y.D. Huang, C.H. Zhang, Y. Wang, T. Wang, The excess loss analysis of an easy-plane FeSiAl@SiO_2 soft magnetic composite with high permeability, J. Magn. Magn Mater. 588 (2023) 171471.
[55] P. Wu, J.H. Cui, K. Wang, Y.D. Huang, L. Qiao, T. Wang, F.S. Li, Study on the influence of the degree of the easy-plane orientation on the high-frequency magnetic properties and power loss of SMC in the MHz band, Acta Mater. 275 (2024) 120041.